

The IceCube Neutrino Observatory

Contributions to ICRC 2015 Part V: Neutrino Oscillations and Supernova Searches

The IceCube Collaboration

Contents

1. Recent Improvements in the Detection of Supernovae with the IceCube Observatory — PoS(ICRC2015)1096 5
2. Search for sterile neutrinos with the IceCube Neutrino Observatory — PoS(ICRC2015)1112 13

*The 34th International Cosmic Ray Conference,
30 July- 6 August, 2015
The Hague, The Netherlands*

IceCube Collaboration Member List

M. G. Aartsen², K. Abraham³², M. Ackermann⁴⁸, J. Adams¹⁵, J. A. Aguilar¹², M. Ahlers²⁹, M. Ahrens³⁹, D. Altmann²³, T. Anderson⁴⁵, I. Ansseau¹², M. Archinger³⁰, C. Argüelles²⁹, T. C. Arlen⁴⁵, J. Auffenberg¹, X. Bai³⁷, S. W. Barwick²⁶, V. Baum³⁰, R. Bay⁷, J. J. Beatty^{17,18}, J. Becker Tjus¹⁰, K.-H. Becker⁴⁷, E. Beiser²⁹, S. BenZvi²⁹, P. Berghaus⁴⁸, D. Berley¹⁶, E. Bernardini⁴⁸, A. Bernhard³², D. Z. Besson²⁷, G. Binder^{8,7}, D. Bindig⁴⁷, M. Bissok¹, E. Blaufuss¹⁶, J. Blumenthal¹, D. J. Boersma⁴⁶, C. Boehm³⁹, M. Börner²⁰, F. Bos¹⁰, D. Bose⁴¹, S. Böser³⁰, O. Botner⁴⁶, J. Braun²⁹, L. Brayeux¹³, H.-P. Bretz⁴⁸, N. Buzinsky²², J. Casey⁵, M. Casier¹³, E. Cheung¹⁶, D. Chirkin²⁹, A. Christov²⁴, K. Clark⁴², L. Classen²³, S. Coenders³², D. F. Cowen^{45,44}, A. H. Cruz Silva⁴⁸, J. Daughhetee⁵, J. C. Davis¹⁷, M. Day²⁹, J. P. A. M. de André²¹, C. De Clercq¹³, E. del Pino Rosendo³⁰, H. Dembinski³³, S. De Ridder²⁵, P. Desiati²⁹, K. D. de Vries¹³, G. de Wasseige¹³, M. de With⁹, T. DeYoung²¹, J. C. Díaz-Vélez²⁹, V. di Lorenzo³⁰, J. P. Dumm³⁹, M. Dunkman⁴⁵, R. Eagan⁴⁵, B. Eberhardt³⁰, T. Ehrhardt³⁰, B. Eichmann¹⁰, S. Euler⁴⁶, P. A. Evenson³³, O. Fadiran²⁹, S. Fahey²⁹, A. R. Fazely⁶, A. Fedynitch¹⁰, J. Feintzeig²⁹, J. Felde¹⁶, K. Filimonov⁷, C. Finley³⁹, T. Fischer-Wasels⁴⁷, S. Flis³⁹, C.-C. Fösig³⁰, T. Fuchs²⁰, T. K. Gaisser³³, R. Gaior¹⁴, J. Gallagher²⁸, L. Gerhardt^{8,7}, K. Ghorbani²⁹, D. Gier¹, L. Gladstone²⁹, M. Glagla¹, T. Glüsenskamp⁴⁸, A. Goldschmidt⁸, G. Golup¹³, J. G. Gonzalez³³, D. Góra⁴⁸, D. Grant²², J. C. Groh⁴⁵, A. Groß³², C. Ha^{8,7}, C. Haack¹, A. Haj Ismail²⁵, A. Hallgren⁴⁶, F. Halzen²⁹, B. Hansmann¹, K. Hanson²⁹, D. Hebecker⁹, D. Heereman¹², K. Helbing⁴⁷, R. Hellauer¹⁶, D. Hellwig¹, S. Hickford⁴⁷, J. Hignight²¹, G. C. Hill², K. D. Hoffman¹⁶, R. Hoffmann⁴⁷, K. Holzapfel³², A. Homeier¹¹, K. Hoshina^{29,a}, F. Huang⁴⁵, M. Huber³², W. Huelsnitz¹⁶, P. O. Hulth³⁹, K. Hultqvist³⁹, S. In⁴¹, A. Ishihara¹⁴, E. Jacobi⁴⁸, G. S. Japaridze⁴, K. Jero²⁹, M. Jurkovic³², B. Kaminsky⁴⁸, A. Kappes²³, T. Karg⁴⁸, A. Karle²⁹, M. Kauer^{29,34}, A. Keivani⁴⁵, J. L. Kelley²⁹, J. Kemp¹, A. Kheirandish²⁹, J. Kiryluk⁴⁰, J. Kläs⁴⁷, S. R. Klein^{8,7}, G. Kohnen³¹, R. Koirala³³, H. Kolanoski⁹, R. Konietz¹, A. Koob¹, L. Köpke³⁰, C. Kopper²², S. Kopper⁴⁷, D. J. Koskinen¹⁹, M. Kowalski^{9,48}, K. Krings³², G. Kroll³⁰, M. Kroll¹⁰, J. Kunnen¹³, N. Kurahashi³⁶, T. Kuwabara¹⁴, M. Labare²⁵, J. L. Lanfranchi⁴⁵, M. J. Larson¹⁹, M. Lesiak-Bzdak⁴⁰, M. Leuermann¹, J. Leuner¹, L. Lu¹⁴, J. Lünemann¹³, J. Madsen³⁸, G. Maggi¹³, K. B. M. Mahn²¹, R. Maruyama³⁴, K. Mase¹⁴, H. S. Matis⁸, R. Maunu¹⁶, F. McNally²⁹, K. Meagher¹², M. Medici¹⁹, A. Meli²⁵, T. Menne²⁰, G. Merino²⁹, T. Meures¹², S. Miarecki^{8,7}, E. Middell⁴⁸, E. Middlemas²⁹, L. Mohrmann⁴⁸, T. Montaruli²⁴, R. Morse²⁹, R. Nahnauer⁴⁸, U. Naumann⁴⁷, G. Neer²¹, H. Niederhausen⁴⁰, S. C. Nowicki²², D. R. Nygren⁸, A. Obertacke⁴⁷, A. Olivas¹⁶, A. Omairat⁴⁷, A. O'Murchadha¹², T. Palczewski⁴³, H. Pandya³³, L. Paul¹, J. A. Pepper⁴³, C. Pérez de los Heros⁴⁶, C. Pfendner¹⁷, D. Pieloth²⁰, E. Pinat¹², J. Posselt⁴⁷, P. B. Price⁷, G. T. Przybylski⁸, J. Pütz¹, M. Quinlan⁴⁵, C. Raab¹², L. Rädcl¹, M. Rameez²⁴, K. Rawlins³, R. Reimann¹, M. Relich¹⁴, E. Resconi³², W. Rhode²⁰, M. Richman³⁶, S. Richter²⁹, B. Riedel²², S. Robertson², M. Rongen¹, C. Rott⁴¹, T. Ruhe²⁰, D. Ryckbosch²⁵, S. M. Saba¹⁰, L. Sabbatini²⁹, H.-G. Sander³⁰, A. Sandrock²⁰, J. Sandroos³⁰, S. Sarkar^{19,35}, K. Schatto³⁰, F. Scheriau²⁰, M. Schimp¹, T. Schmidt¹⁶, M. Schmitz²⁰, S. Schoenen¹, S. Schöneberg¹⁰, A. Schönwald⁴⁸, L. Schulte¹¹, D. Seckel³³, S. Seunarine³⁸, R. Shanidze⁴⁸, M. W. E. Smith⁴⁵, D. Soldin⁴⁷, M. Song¹⁶, G. M. Spiczak³⁸, C. Spiering⁴⁸, M. Stahlberg¹, M. Stamatikos^{17,b}, T. Stanev³³, N. A. Stanisha⁴⁵, A. Stasik⁴⁸, T. Stezelberger⁸, R. G. Stokstad⁸, A. Stöbl⁴⁸, R. Ström⁴⁶, N. L. Strotjohann⁴⁸, G. W. Sullivan¹⁶, M. Sutherland¹⁷, H. Taavola⁴⁶, I. Taboada⁵, S. Ter-Antonyan⁶, A. Terliuk⁴⁸, G. Tešić⁴⁵, S. Tilav³³, P. A. Toale⁴³, M. N. Tobin²⁹, S. Toscano¹³, D. Tosi²⁹, M. Tselengidou²³, A. Turcati³², E. Unger⁴⁶, M. Usner⁴⁸, S. Vallecorsa²⁴, J. Vandenbroucke²⁹, N. van Eijndhoven¹³,

S. Vanheule²⁵, J. van Santen²⁹, J. Veenkamp³², M. Vehring¹, M. Voge¹¹, M. Vraeghe²⁵, C. Walck³⁹, A. Wallace², M. Wallraff¹, N. Wandkowsky²⁹, Ch. Weaver²², C. Wendt²⁹, S. Westerhoff²⁹, B. J. Whelan², N. Whitehorn²⁹, C. Wichary¹, K. Wiebe³⁰, C. H. Wiebusch¹, L. Wille²⁹, D. R. Williams⁴³, H. Wissing¹⁶, M. Wolf³⁹, T. R. Wood²², K. Woschnagg⁷, D. L. Xu⁴³, X. W. Xu⁶, Y. Xu⁴⁰, J. P. Yanez⁴⁸, G. Yodh²⁶, S. Yoshida¹⁴, M. Zoll³⁹

¹III. Physikalisches Institut, RWTH Aachen University, D-52056 Aachen, Germany

²Department of Physics, University of Adelaide, Adelaide, 5005, Australia

³Dept. of Physics and Astronomy, University of Alaska Anchorage, 3211 Providence Dr., Anchorage, AK 99508, USA

⁴CTSPS, Clark-Atlanta University, Atlanta, GA 30314, USA

⁵School of Physics and Center for Relativistic Astrophysics, Georgia Institute of Technology, Atlanta, GA 30332, USA

⁶Dept. of Physics, Southern University, Baton Rouge, LA 70813, USA

⁷Dept. of Physics, University of California, Berkeley, CA 94720, USA

⁸Lawrence Berkeley National Laboratory, Berkeley, CA 94720, USA

⁹Institut für Physik, Humboldt-Universität zu Berlin, D-12489 Berlin, Germany

¹⁰Fakultät für Physik & Astronomie, Ruhr-Universität Bochum, D-44780 Bochum, Germany

¹¹Physikalisches Institut, Universität Bonn, Nussallee 12, D-53115 Bonn, Germany

¹²Université Libre de Bruxelles, Science Faculty CP230, B-1050 Brussels, Belgium

¹³Vrije Universiteit Brussel, Dienst ELEM, B-1050 Brussels, Belgium

¹⁴Dept. of Physics, Chiba University, Chiba 263-8522, Japan

¹⁵Dept. of Physics and Astronomy, University of Canterbury, Private Bag 4800, Christchurch, New Zealand

¹⁶Dept. of Physics, University of Maryland, College Park, MD 20742, USA

¹⁷Dept. of Physics and Center for Cosmology and Astro-Particle Physics, Ohio State University, Columbus, OH 43210, USA

¹⁸Dept. of Astronomy, Ohio State University, Columbus, OH 43210, USA

¹⁹Niels Bohr Institute, University of Copenhagen, DK-2100 Copenhagen, Denmark

²⁰Dept. of Physics, TU Dortmund University, D-44221 Dortmund, Germany

²¹Dept. of Physics and Astronomy, Michigan State University, East Lansing, MI 48824, USA

²²Dept. of Physics, University of Alberta, Edmonton, Alberta, Canada T6G 2E1

²³Erlangen Centre for Astroparticle Physics, Friedrich-Alexander-Universität Erlangen-Nürnberg, D-91058 Erlangen, Germany

²⁴Département de physique nucléaire et corpusculaire, Université de Genève, CH-1211 Genève, Switzerland

²⁵Dept. of Physics and Astronomy, University of Gent, B-9000 Gent, Belgium

²⁶Dept. of Physics and Astronomy, University of California, Irvine, CA 92697, USA

²⁷Dept. of Physics and Astronomy, University of Kansas, Lawrence, KS 66045, USA

²⁸Dept. of Astronomy, University of Wisconsin, Madison, WI 53706, USA

²⁹Dept. of Physics and Wisconsin IceCube Particle Astrophysics Center, University of Wisconsin, Madison, WI 53706, USA

³⁰Institute of Physics, University of Mainz, Staudinger Weg 7, D-55099 Mainz, Germany

- ³¹Université de Mons, 7000 Mons, Belgium
- ³²Technische Universität München, D-85748 Garching, Germany
- ³³Bartol Research Institute and Dept. of Physics and Astronomy, University of Delaware, Newark, DE 19716, USA
- ³⁴Dept. of Physics, Yale University, New Haven, CT 06520, USA
- ³⁵Dept. of Physics, University of Oxford, 1 Keble Road, Oxford OX1 3NP, UK
- ³⁶Dept. of Physics, Drexel University, 3141 Chestnut Street, Philadelphia, PA 19104, USA
- ³⁷Physics Department, South Dakota School of Mines and Technology, Rapid City, SD 57701, USA
- ³⁸Dept. of Physics, University of Wisconsin, River Falls, WI 54022, USA
- ³⁹Oskar Klein Centre and Dept. of Physics, Stockholm University, SE-10691 Stockholm, Sweden
- ⁴⁰Dept. of Physics and Astronomy, Stony Brook University, Stony Brook, NY 11794-3800, USA
- ⁴¹Dept. of Physics, Sungkyunkwan University, Suwon 440-746, Korea
- ⁴²Dept. of Physics, University of Toronto, Toronto, Ontario, Canada, M5S 1A7
- ⁴³Dept. of Physics and Astronomy, University of Alabama, Tuscaloosa, AL 35487, USA
- ⁴⁴Dept. of Astronomy and Astrophysics, Pennsylvania State University, University Park, PA 16802, USA
- ⁴⁵Dept. of Physics, Pennsylvania State University, University Park, PA 16802, USA
- ⁴⁶Dept. of Physics and Astronomy, Uppsala University, Box 516, S-75120 Uppsala, Sweden
- ⁴⁷Dept. of Physics, University of Wuppertal, D-42119 Wuppertal, Germany
- ⁴⁸DESY, D-15735 Zeuthen, Germany
- ^aEarthquake Research Institute, University of Tokyo, Bunkyo, Tokyo 113-0032, Japan
- ^bNASA Goddard Space Flight Center, Greenbelt, MD 20771, USA

Acknowledgment: We acknowledge the support from the following agencies: U.S. National Science Foundation-Office of Polar Programs, U.S. National Science Foundation-Physics Division, University of Wisconsin Alumni Research Foundation, the Grid Laboratory Of Wisconsin (GLOW) grid infrastructure at the University of Wisconsin - Madison, the Open Science Grid (OSG) grid infrastructure; U.S. Department of Energy, and National Energy Research Scientific Computing Center, the Louisiana Optical Network Initiative (LONI) grid computing resources; Natural Sciences and Engineering Research Council of Canada, WestGrid and Compute/Calcul Canada; Swedish Research Council, Swedish Polar Research Secretariat, Swedish National Infrastructure for Computing (SNIC), and Knut and Alice Wallenberg Foundation, Sweden; German Ministry for Education and Research (BMBF), Deutsche Forschungsgemeinschaft (DFG), Helmholtz Alliance for Astroparticle Physics (HAP), Research Department of Plasmas with Complex Interactions (Bochum), Germany; Fund for Scientific Research (FNRS-FWO), FWO Odysseus programme, Flanders Institute to encourage scientific and technological research in industry (IWT), Belgian Federal Science Policy Office (Belspo); University of Oxford, United Kingdom; Marsden Fund, New Zealand; Australian Research Council; Japan Society for Promotion of Science (JSPS); the Swiss National Science Foundation (SNSF), Switzerland; National Research Foundation of Korea (NRF); Danish National Research Foundation, Denmark (DNRF)

Recent Improvements in the Detection of Supernovae with the IceCube Observatory

The IceCube Collaboration[†],

[†] http://icecube.wisc.edu/collaboration/authors/icrc15_icecube

E-mail: Volker.Baum@icecube.wisc.edu

IceCube monitors one cubic kilometer of deep Antarctic ice with a lattice of 5160 optical sensors in search of neutrino signals from supernovae. Charge secondaries arising from neutrino interactions in the ice produce Cherenkov photons that are registered by photomultipliers in the sensors. Due to subfreezing ice temperatures, their dark rates are particularly low. Therefore a collective rate enhancement introduced by interacting neutrinos in all photomultipliers provides excellent sensitivity for core collapse supernovae of galactic origin. A detailed understanding of the characteristics and temporal changes of the dark rate background has been achieved and cosmic ray induced muons, responsible for the majority of fake supernova candidate triggers, are rejected in real time. An addition to the standard data acquisition allows IceCube to buffer all registered photons in the detector in case of a serious alert. By analyzing such data, a precision determination of the burst onset time and the characteristics of rapidly varying fluxes, as well as estimates of the average neutrino energies and - for supernovae ending in a black hole - of the burst direction may be obtained. Such data are also crucial to characterize details of the noise behavior and of the atmospheric muon background.

Corresponding authors: V. Baum^{*1}, B. Eberhardt¹, A. Fritz¹, D. Heereman², B. Riedel³

¹ *Institute of Physics, University of Mainz*

² *Interuniversity Institute for High Energies, Université Libre de Bruxelles, Belgium*

³ *Department of Physics, University of Alberta, Canada*

*The 34th International Cosmic Ray Conference,
30 July- 6 August, 2015
The Hague, The Netherlands*

^{*}Speaker.

1. Introduction

IceCube, a grid of 5160 photo sensors imbedded in the ice of the Antarctic glacier, is uniquely suited to monitor our Galaxy for supernovae due to its 1 km^3 size and its location. In the inert and -43°C to -20°C cold ice, IceCube's photomultiplier noise rates average around 540 Hz. At depths between 1450 – 2450 m, the detector is partly shielded from cosmic ray induced muons. The inverse beta process $\bar{\nu}_e + p \rightarrow e^+ + n$ dominates supernova neutrino interactions with $\mathcal{O}(10 \text{ MeV})$ energy in ice, leading to positron tracks of about $0.6 \text{ cm} \cdot E_\nu / \text{MeV}$ length which radiate $178 \cdot E_{e^+} / \text{MeV}$ Cherenkov photons in the 300 – 600 nm wavelength range. From the approximate E_ν^2 dependence of the cross section and the linear energy dependence of the track length, the light yield per neutrino roughly scales with E_ν^3 . With absorption lengths exceeding 100 m, photons travel long distances in the ice so that each DOM effectively monitors several hundred cubic meters of ice. Typically, only a single photon from each interaction reaches one of the photomultipliers that are vertically (horizontally) separated by roughly 17 m (125 m). The DeepCore subdetector, equipped with a denser array of high efficiency photomultipliers, provides higher detection and coincidence probabilities.

Although the rate increase in individual light sensors is not statistically significant, the effect will be clearly seen once the rise is considered collectively over many sensors. IceCube is the most precise detector for analyzing the neutrino light curve of close supernovae [1]. Since 2009, IceCube has been sending real-time data grams to the Supernova Early Warning System (SNEWS) [2] when detecting supernova candidate events. The supernova data acquisition is based on count rates of individual optical modules stored in 1.6384 ms time bins. The analysis framework calculates the average dark noise rate deviation $\Delta\mu$ normalized to its own width $\sigma_{\Delta\mu}$ and calculates for each candidate the significance $\xi = \Delta\mu / \sigma_{\Delta\mu}$. In addition, all time-stamped hits in the detector are buffered and extracted for supernova candidate triggers (hitspooling) [3].

In this paper, we first characterize the effect of the atmospheric muon background and introduce a subtraction method for the associated hits. We then discuss in detail the properties of the photomultiplier dark noise on top of which the supernova neutrino signal would be observed and we will finally quantify the directional resolution that can be obtained for a class of supernovae that abruptly form a black hole.

2. Improved significance calculation by correcting for atmospheric muon hits

Atmospheric muons require an energy of $\approx 400 \text{ GeV}$ at the surface to reach the detector (see Fig. 1, left) and $\approx 550 \text{ GeV}$ to trigger the IceCube 8-fold majority trigger; hits from muon tracks that fail the trigger requirements are mostly found in the upper detector layers or are corner clippers (see Fig. 1, right). Dust layers in the ice, particularly the one $\approx 100 \text{ m}$ below the detector center, absorb light. This effect and the limited muon range lead to a depth-dependent atmospheric muon induced rate between $\approx 3 \text{ Hz}$ and $\approx 30 \text{ Hz}$. While the fraction of such hits in each DOM is small compared to its dark rate, the effect on the summed hits as well as on the significance ξ to observe a rate excess in all optical modules is much more apparent [4]. The reason is that muons lead to space and time correlated hits such that the optical sensor rates are not statistically independent and

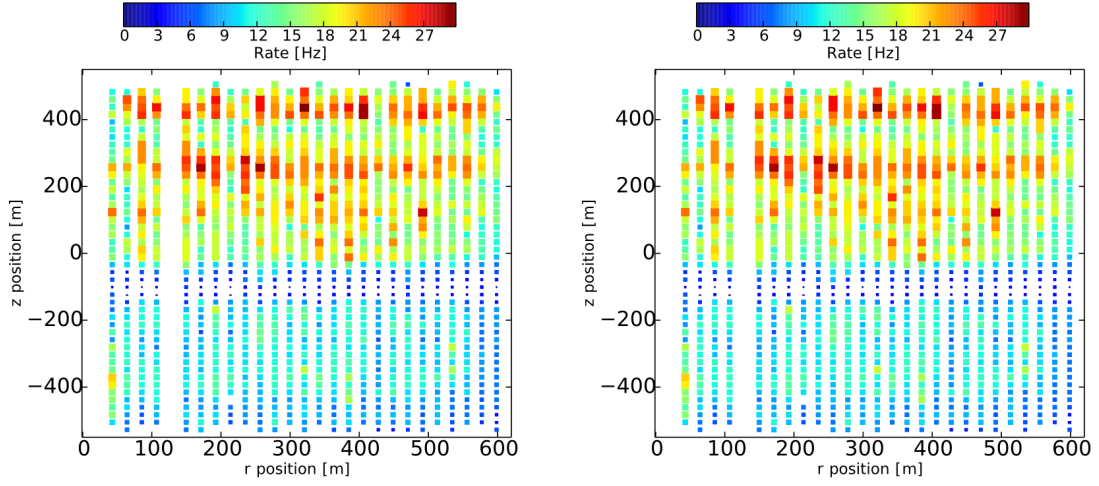


Figure 1: Simulated muon induced hit rates as function of horizontal position and radius w.r.t. to the detector center at 1950 m depth. *Left*: all hits associated with muons triggering the detector. *Right*: hits associated with muons not meeting any trigger condition.

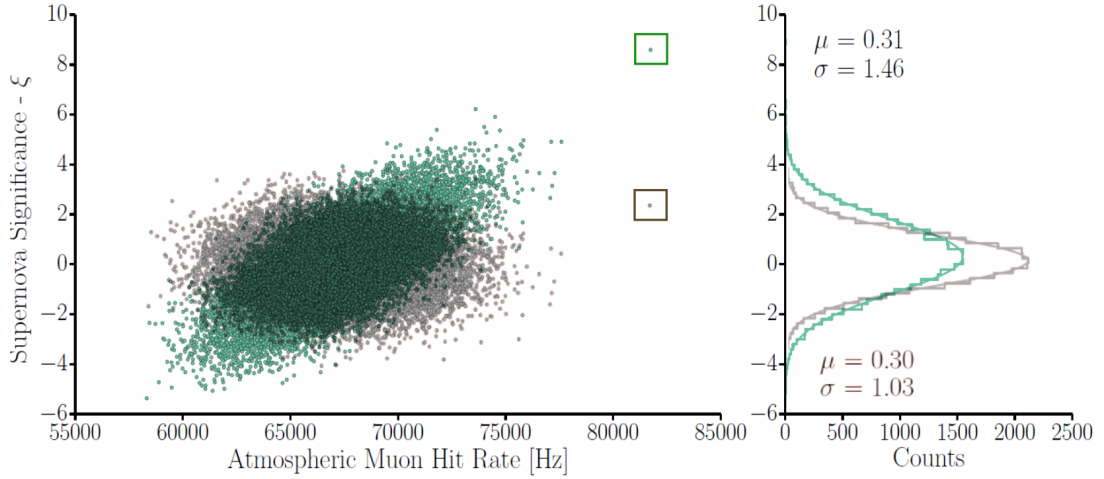


Figure 2: Correlation of the atmospheric muon induced hit rate with the significance ξ (green). The application of the decorrelation discussed in the text leads to the gray distribution. The projections on the right hand side demonstrate the sharpening of the significance distribution after decorrelation. During this particular run, the highest significant candidate so far was observed (marked by a green square). After decorrelation, the significance dropped (marked by a gray square) verifying that the candidate was due to an upward fluctuation in the number of atmospheric muon hits.

the law of large numbers is no longer applicable. In fact, the vast majority of false positive triggers are due to statistical agglomerations of atmospheric muon induced hits.

In case of an alert, the only independent quantity to check whether the event was real or spurious is the cosmic ray induced muon activity during the respective period. We demonstrated in an offline analysis [4] that the separation of signal from background can be considerably improved by subtracting hits associated to atmospheric muon induced tracks. The subtraction method fits

a linear function to the correlation between the simple majority trigger hit rate R_{μ}^{hit} as a measure for the atmospheric muon rate and the significance ξ (see Fig. 2 for an example 8 hour run) and calculates a corrected significance $\xi' = \xi - b \cdot R_{\mu}^{\text{hit}} - a$ from the resulting offset a and slope b . This method lowers the significance of the sample alert from $\xi = 8.59$ to $\xi' = 2.44$ and decreases the width of the significance distribution from 1.46 to 1.03, close to the expectation of unity for uncorrelated noise. Until recently, such a study could only be performed offline with a few days delay due to limited satellite time availability and bandwidth. In order to perform an atmospheric muon correction in real time, the number of hits processed by IceCube's majority trigger is transmitted to the supernova data acquisition system. To guarantee a robust system and to limit the increase in processing time, the data are only processed once a predefined significance threshold ξ_{cut} is crossed. The method reduces the number of fake alarms by almost three orders of magnitude when keeping the same alarm threshold as before. The additional memory and CPU requirements do not affect the stability of the system so that one may now lower the alarm thresholds. By applying a cut on $\xi > 4.0$ before atmospheric muon subtraction one does already achieve a factor of 10^{-2} in background reduction compared to the original threshold of $\xi > 7.65$ (see Fig. 3) which further improves to about 10^{-7} by switching to the combination $\xi > 4.0, \xi' > 5.6$. Using this combination we are also able to increase the SNEWS alarm efficiency for potential supernovae in the Large Magellanic Cloud from merely 12% to 82%, while meeting the SNEWS requirement to sent alarms with a frequency of less than one alarm per 10 days.

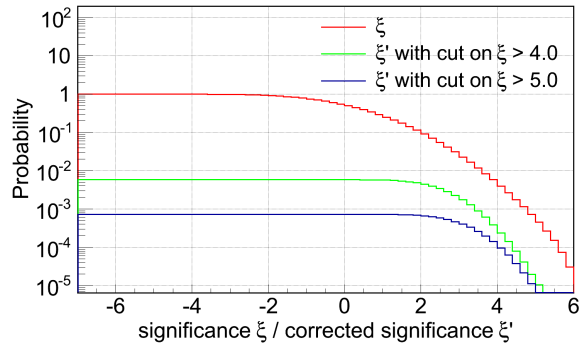


Figure 3: Cumulative probabilities to detect an event with significance ξ (red) and to detect the corrected significance ξ' after additional cuts on ξ (Cuts shown are $\xi > 4.0$ and $\xi > 5.0$ in green and blue.)

3. Long term behavior of DOM dark rates

Over the course of the first three years of the completed detector (IC86-2011, IC86-2012, IC86-2013), the number of false positive supernova alerts increased by almost 50% with time. This came as a surprise as we did not expect the sensitivity to cosmic ray induced muons to increase while the detector configuration remained unchanged. As can be seen from Fig. 4, the average dark noise rate of the optical modules decreased with time, on average, by 3.5%. This decrease led to an increased sensitivity to atmospheric muons of $\approx 2\%$ and - as discussed above - to a disproportional increase in the false positive trigger rate. The decrease in the dark noise rate is correlated with the deployment date and the depth of the DOMs. It is particularly evident in the lower, warmer section of the detector, where the pressure is highest and the ice is under mechanical stress. While no definite source could be established, we suspect that the emission of light is caused by triboluminescence caused by the freezing of the ice in the bore holes.

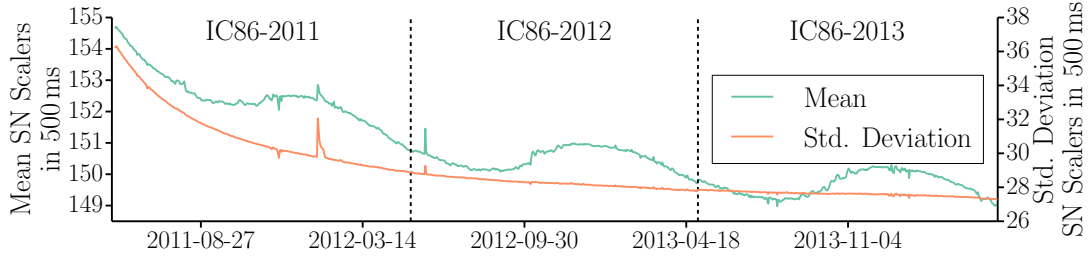


Figure 4: Temporal development of the mean SN scaler rate and standard deviation in 500 ms time bins after applying an artificial dead time of $250 \mu\text{s}$. Both, seasonal varying influence of atmospheric muons and an overall decrease in the dark rate, are apparent in the mean rate (blue curve), while the standard deviation is rather insensitive to the influence of muons (orange curve). The rate spikes are detector related; in particular, the dark rate increased after light was emitted during the operation of a camera in the deep ice in early 2012.

4. Exploiting detailed information from spooling all hits

when taking into account the larger uncertainty on the moving average noise determination when using the 90 s long hitspooling data fragment rather than the 10 min available in the scaler based data acquisition system. The detailed information available in the hitspooling data can be exploited for several purposes, some of which we will discuss below:

- basic studies of the non-Poissonian characteristics of dark noise at low temperatures,
- characterization of the dark noise for individual sensors to improve IceCube’s Monte Carlo simulations,
- application of sophisticated techniques to identify noise hits or hits associated with atmospheric muons that do not trigger the IceCube majority trigger,
- determination of coincidence probabilities for the estimation of the average supernova neutrino energy [5], and
- triangulation of the supernova direction in the case that signals change abruptly.

Non-Poissonian noise characteristics: Hitspooling data were used to investigate the characteristics of correlated dark noise that rises at low temperatures and compare in-ice measurements with those taken in the laboratory. Figure 5 shows the IceCube dark rate as function of depth-dependent temperature at the PMT photo cathodes. Each data point represents the average of 12 optical module layers with DeepCore excluded; ref. [6] was used to translate the known depth into an ice temperature. Correlated noise, suspected to be due to glass fluorescence, comes in bursts, while uncorrelated noise follows a Poissonian distribution. By defining a burst as an uninterrupted sequence of < 3 ms intervals, the number of hits L present in the burst, the frequency of burst F_L with a given number of hits, the time between the last and the first hit in a burst D_L , and the inter-burst interval distribution were measured and compared to previous results by Meyer [7]. The average number of hits per burst rises roughly linearly from 3.3 hits at -10°C to 3.8 hits at -33°C . Figures 6, left and right, show the corresponding distributions which are in general in agreement with the findings of [7]. For instance, the average burst duration D_L follows Meyer’s anticipation

of a power law proportional to $L^{1/2}$ with the difference that we identify two separate regions for best fits.

Improved muon identification and rejection: Simulation data show that $\sim 50\%$ of all atmospheric muons crossing the detector are triggered. The remaining half leads to a factor of three fewer hits mostly at the top of the detector (see Fig.1, right); 26 % of all subthreshold muons produce only a single hit in the detector. Removing these subthreshold muons hits may be achieved by restricting oneself to hits in the lower part of the detector or by using algorithms developed to identify hits clustering in time and space combined with an investigation of the multiplicity of track segments formed by each pair of hits in the cluster. With the second method, it is possible to identify up to 45 % of all sub-threshold muons hits, limited only by the requirement of at least 4 hits to define a cluster in the algorithms.

Applying these techniques to experimental data results in a $\sim 3\%$ decrease of the total hit rate and reduces the fraction of false positive SNEWS alarms by an additional 45%. In the future, we will use this improvement in the determination of the average neutrino energy.

Triangulation of supernova direction: IceCube cannot identify individual neutrino interactions as usually only one photon is detected per interaction. In addition, the direction of the positron is essentially uncorrelated with the incoming neutrino direction for the dominant inverse beta decay interaction. Therefore it is a challenge to measure the supernova direction with IceCube. Triangulation with other detectors has been proposed [8, 9] as one possibility. Another option is to determine the direction from the temporal hit pattern seen in the cubic-kilometer detector when a neutrino wavefront changing its intensity abruptly. The detector crossing lasts only several mi-

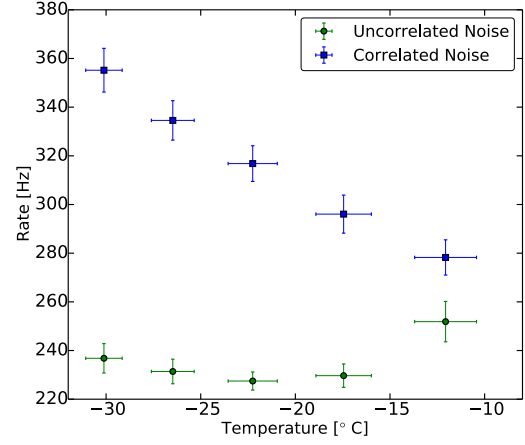


Figure 5: Non-Poissonian correlated and Poissonian uncorrelated components of IceCube's dark rate as function of the estimated temperature close to the PMT cathode.

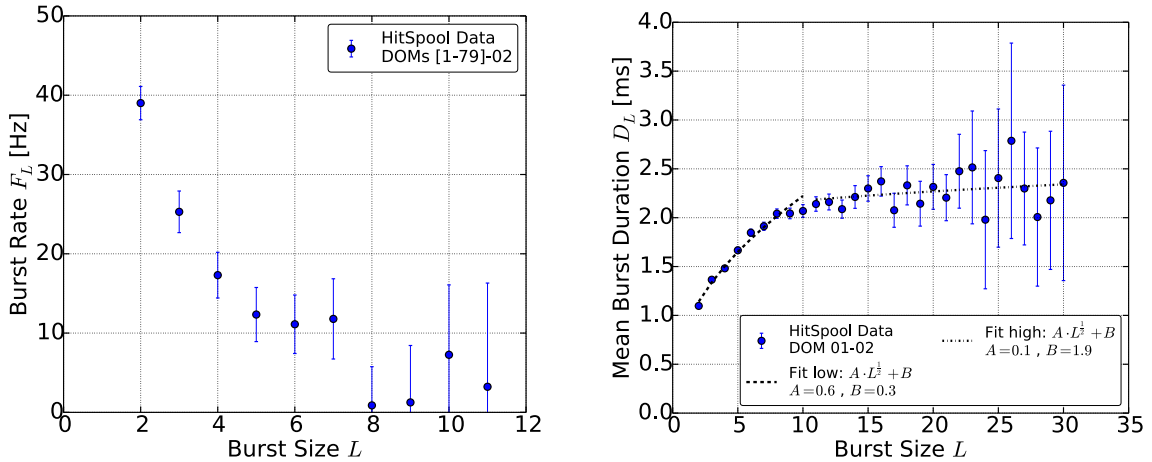


Figure 6: Burst rate F_L (left) and average burst duration D_L (right) as function of burst size L .

croseconds, which sets the time-scale for abrupt flux change to be suitable.

One example is the formation of a black hole following a core collapse of a super-massive star. In case the protoneutron star forms a black hole instead of gradually cooling as a stable neutron star, the neutrino flux should cease almost immediately, once the Schwarzschild condition is met [10]. The neutrino fluxes may also gradually decrease as more and more matter in the star approaches the event horizon and the gravitational redshift becomes extremely strong [11] (see green curve in Fig. 7). In addition, the neutrinos follow a spectrum of energies, which - due to the non-vanishing neutrino masses - leads to a smearing of the time arrival distribution (see Fig. 7). Black holes forming core collapse supernovae have therefore been suggested as a way to determine the neutrino mass [10]. We first adopt the optimistic scenario that the smearing due to the black hole dynamics is negligible [12]. An unbinned likelihood analysis with an optimized minimizer is used to determine the direction from the timing pattern of the hit DOMs. Figure 8 shows the simulated resolution achieved as function of distance (left) and as function of neutrino masses (right). Obviously, reasonable directional resolution can be achieved only for close-by supernovae and low neutrino masses.

Using the assumption of a gradual decrease of neutrino luminosity [11] and numerically folding the distribution of [10] for the time-delay due to finite neutrino masses, one finds that directions can only be reconstructed for very close supernovae.

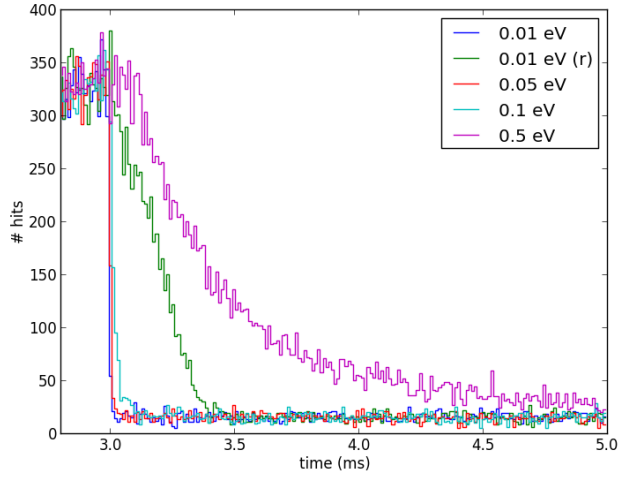


Figure 7: Effect of neutrino mass on the observed neutrino flux for abrupt black hole creation. The green line shows the effect of a gradual decrease of the neutrino luminosity ($m_\nu = 0.01$ eV).

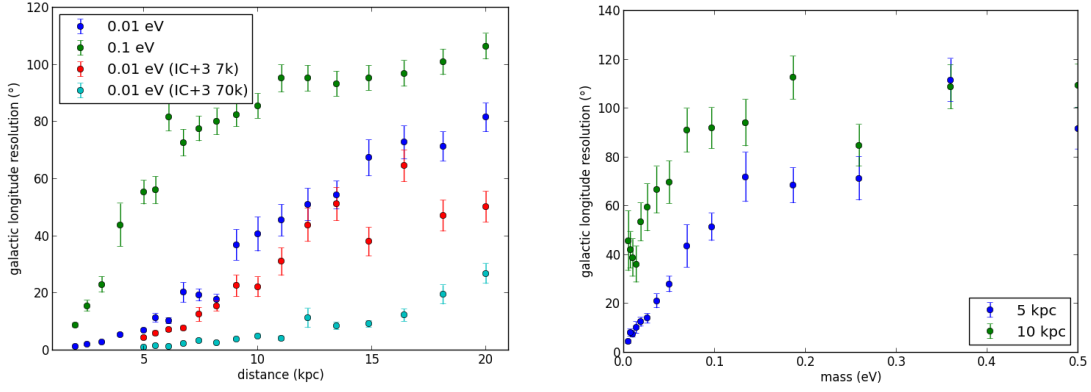


Figure 8: *Left:* Resolution in galactic longitude achievable by triangulation within IceCube’s geometry for a supernova with abrupt black hole formation for two assumptions on the mass of the lightest neutrino as well as for a hypothetical detector extension with 3 additional strings deployed symmetrically around the IceCube’s center at 7 and 70 km distance. *Right:* Resolution in galactic longitude as function of neutrino mass.

5. Conclusions and Outlook

The IceCube observatory provides the world’s best statistical accuracy for the neutrino flux of supernovae in our galaxy with a round-the-clock up-time of close to 99%. However, energies and directions of individual neutrinos can not be determined due to the optical sensor dark rates and - to a lesser extend - due to atmospheric muons passing the detector. Therefore it is very important to understand the dark rate and atmospheric muon characteristics. Neutrino energies and the supernova direction can be determined statistically when analyzing the timing information of all hits in the detector. In the future, the sensitivity to the absolute neutrino mass will be assessed, the energy determination will be improved, the idea of analyzing $\mathcal{O}(10)$ s long bursts will be extended to shorter potential signals, and the hitspooling system will be used for other use cases, such as the estimate of hadronic energy in highly energetic events from the delayed neutron capture signal.

References

- [1] R. Abbasi *et al.* (IceCube Collaboration), *A&A* **535** (2011) A109.
- [2] P. Antonioli *et al.*, *New J. Phys.* **6** (2004) 114.
- [3] D. Heereman, V. Baum, G. Kroll, and B. Riedel (IceCube Collaboration), contribution to the 33rd International Cosmic Ray Conference, arXiv:1309.7008 [astro-ph.HE].
- [4] V. Baum, B. Eberhardt, G. Kroll, and B. Riedel (IceCube Collaboration), contribution to the 33rd International Cosmic Ray Conference, arXiv:1309.7008 [astro-ph.HE].
- [5] R. Bruijn, *Nucl. Phys. B Proc. Supp.* **00** (2012) 13.
- [6] P. Buford Price *et al.*, *Proceedings of the National Academy of Sciences* **99** (2002) 12:7844.
- [7] H.O. Meyer, *EPL* **89** (2010) 58001.
- [8] R. Tomas, D. Semikoz, G.G. Raffelt, M. Kachelriess, and A.S. Dighe, *Phys. Rev. D* **68** (2003) 093013.
- [9] T. Mühlbeier, H. Nunokawa and R. Zukanovich Funchal, *Phys. Rev. D* **88** (2013) 085010.
- [10] J.F. Beacom, R.N. Boyd, and A. Mezzacappa, *Phys. Rev. D* **63** (2001) 073011.
- [11] T.E. Baumgarte, S.L. Shapiro, S.A. Teukolsky, *Astrophys.J.* **458** (1996) 680.
- [12] K. Sumiyoshi, S. Yamada and H. Suzuki, *Astrop.J.* **667** (2007) 382.

Search for sterile neutrinos with the IceCube Neutrino Observatory

The IceCube Collaboration[†]

[†] http://icecube.wisc.edu/collaboration/authors/icrc15_icecube

E-mail: marius.wallraff@physik.rwth-aachen.de

The IceCube Neutrino Observatory is a 1 km^3 Cherenkov detector located at the geographic South Pole. It records several tens of thousands high-energy atmospheric muon neutrino events per year, with energies between about one hundred GeV and several tens of TeV. This allows a precise measurement of the energy and angular distributions and a search for deviations from the standard expectation that could be due to new physics.

If additional sterile neutrino states exist with mass differences on the order of 1 eV and mix with muon neutrinos, IceCube would observe a deficit compared to the expected neutrino rate in the energy range of a few TeV due to strong matter effects in the neutrino propagation through Earth. The disappearance depends on the energy and the path of the neutrino through the Earth and thus its zenith angle.

Here, we report on the first exploratory effort to make use of this resonance effect to substantially improve the sensitivity with respect to searches that are based on vacuum oscillations. This paper describes results that are based on a large muon neutrino sample measured by IceCube between 2009 and 2010 in its 59-string configuration.

Corresponding authors: M. Wallraff^{1*}, C. Wiebusch¹

¹ *III. Physikalisches Institut, RWTH Aachen University*

*The 34th International Cosmic Ray Conference,
30 July- 6 August, 2015
The Hague, The Netherlands*

*Speaker.

1. Introduction

After many decades of research, neutrino flavor oscillations are still an active area of experimental measurements for particle and astroparticle physics. Despite the elusive nature of neutrinos, most parameters that govern the oscillations between the three known neutrino flavors are well known today [1].

Several experimental anomalies, most prominently the $\bar{\nu}_\mu \rightarrow \bar{\nu}_e$ measurements of the two neutrino beam experiments LSND [2] and MiniBooNE [3], indicate that there could be effects that can not be explained well with the current model of three active neutrinos. One way to explain these measurements is to modify the model by addition of new flavors of neutrinos with a typical mass difference of $\Delta m_{42}^2 \approx 1 \text{ eV}^2$. To prevent contradictions to various older measurements such as the well-known limit on the number of light neutrinos from Z_0 branching ratio measurements at the LEP [4], these new flavors can not participate in weak interactions and are therefore called sterile [5]. As sterile neutrinos can mix with the active neutrinos, their existence can be tested by the search for disappearance of active neutrinos.

2. The IceCube Neutrino Observatory

The IceCube Neutrino Observatory is a neutrino detector located at the Amundsen-Scott South Pole Station. It uses the naturally clear ice of Antarctica as optical medium to observe Cherenkov radiation emitted by charged leptons that have been created by neutrino interactions in the ice. Its active volume of about one cubic kilometer lies at a depth of about 1.5 to 2.5 km beneath the surface of the ice and is instrumented with 5160 digital optical modules (DOMs) distributed over 86 vertical cables called strings. IceCube was completed in December 2010, but it has already been taking data in the years before with the partially completed detector. The analysis presented here was conducted on data taken with the 59-string configuration between May 2009 and May 2010, called IC-59. This data set consists of approximately 22 000 up-going track-like events from charged-current muon neutrino interactions that have good reconstruction quality and energies between about 100 GeV and 50 TeV. For details about the event selection, see [6]. A second independent IceCube analysis of comparable sensitivity is close to completion, using the first year of data taken with the final 86-string configuration, and will be reported soon.

3. Sterile Neutrino Signatures in IceCube

This analysis is searching for the resonant disappearance of atmospheric muon neutrinos caused by matter-enhanced oscillations during propagation through Earth [7]. For illustrative purposes, the oscillation probability of muon neutrinos to an additional sterile neutrino flavor can be approximated by a two-flavor formalism in the relevant parameter range. The vacuum oscillation probability is then described by

$$P_{\nu_\mu \rightarrow \nu_s} = \sin^2(2\theta_{24}) \sin^2 \left(1.267 \frac{\Delta m_{42}^2 L}{E_\nu} \frac{\text{GeV}}{\text{eV}^2 \text{ km}} \right),$$

where θ_{24} is the mixing angle between muon neutrinos and sterile neutrinos and Δm_{42}^2 the difference between their squared masses. E_ν is the neutrino energy and L the baseline, i.e., the distance

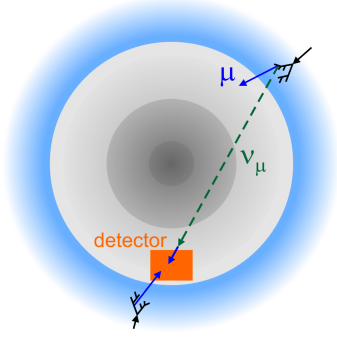


Figure 1: Path of a muon neutrino created in the atmosphere (blue) through Earth, shaded according to density.

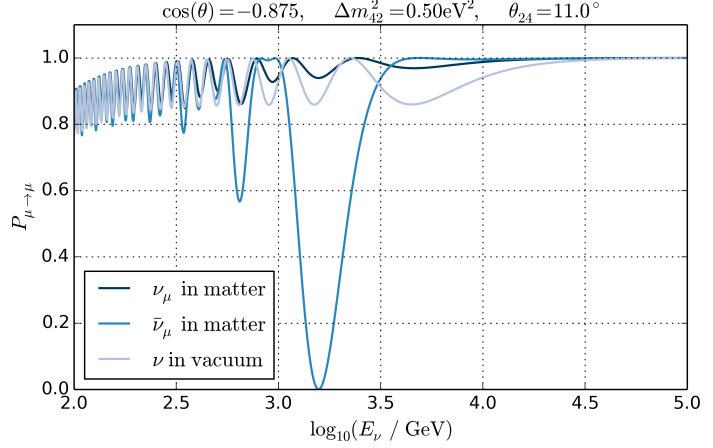


Figure 2: Oscillation probabilities for the neutrino path shown in fig. 1 as a function of its energy in a 3+1 model.

the neutrino traveled after its creation. The baseline can be calculated from the zenith angle θ under which the muon travels through the detector (fig. 1). For up-going atmospheric neutrinos, it lies between 500 km for near-horizontal trajectories and 12 800 km, which is the Earth diameter including the atmosphere, for vertical trajectories.

An important difference when compared to conventional atmospheric neutrino analyses is that matter effects inside the Earth are strong. The three conventional flavors can scatter on nucleons and electrons by neutral-current (NC) interactions, and electron neutrinos can additionally scatter elastically on electrons by charged-current (CC) interactions. Sterile neutrinos can not interact weakly by construction. This induces effective mass differences between the flavors that depend on the electron and neutron particle densities. For more detail, see [8]. These induced effective mass differences can cause strong resonances at which the disappearance becomes much stronger than the mixing angle would allow in vacuum. An example is shown in fig. 2. For a new mass state of larger mass than the three known states ($0 < \Delta m_{32}^2 < \Delta m_{42}^2$) and without CP violation, the resonance enhances the oscillations in the antineutrino channel and suppresses them for neutrinos. Above 100 GeV, the flux of muon neutrinos is larger than that of muon antineutrinos. For this reason, the case described above is the most pessimistic for IceCube and was therefore selected as basis for this initial analysis. It is important to note that the oscillation appears according to the effective mixing as a resonance-like effect, even for small values of vacuum mixing. Therefore, the measurement of atmospheric neutrinos in the relevant energy range has a high sensitivity also to small mixing angles, where vacuum oscillations are small.

The analysis itself does not employ two-flavor approximations, but instead uses full four-flavor propagation based on numeric calculations with the tool nuCraft [9]. The rotation matrix with θ_{24} has been multiplied to the left side of the 4×4 PMNS matrix. All other sterile mixing angles have been set to zero; θ_{14} controls the mixing between electron and sterile neutrinos and is negligible for the atmospheric muon neutrino disappearance as seen by IceCube. For non-zero θ_{24} , the tau-sterile angle θ_{34} influences oscillation amplitude and shape roughly similar to θ_{24} [10]. It also results in a substantial fraction of the muon neutrinos oscillating to tau neutrinos instead of sterile neutrinos. However, most tau neutrinos cause cascade-like signatures and the

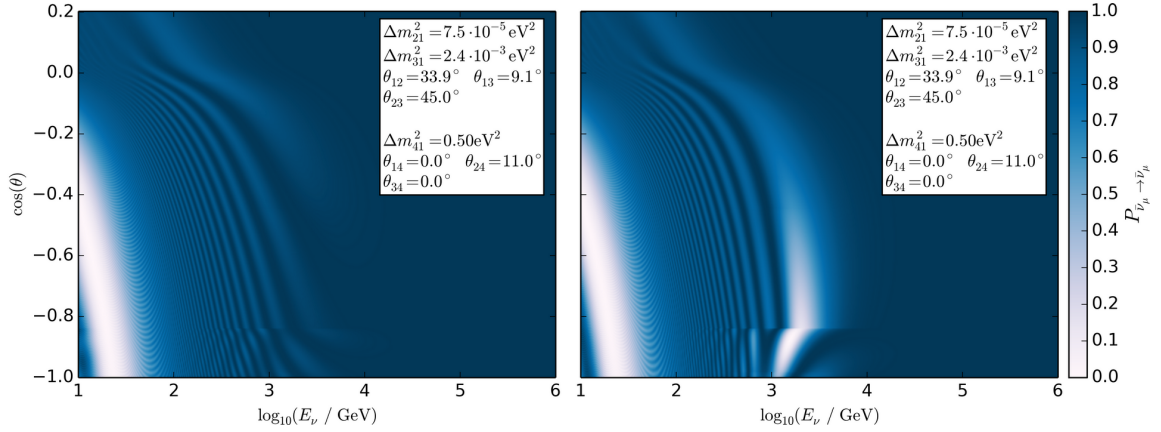


Figure 3: Probability for atmospheric muon neutrinos (left) and muon antineutrinos (right) for the particle to reach the detector in the same state, with one sterile state of neutrinos, parameters as specified in the plot.

remaining 15% produce only faint muon tracks, so they are strongly suppressed by this event selection, which favors track-like signatures. For these reasons, $\theta_{34} \neq 0$ leads to signatures that are sufficiently similar to (and stronger than) those with $\theta_{34} = 0$ to warrant this parameter to be omitted for now. Also, models with more than one sterile flavor have not been included into this analysis to keep it computationally feasible. The signatures of models with multiple sterile flavors can be approximated well by superpositions of 3+1 signatures and are therefore much more similar to 3+1 models than to 3+0 models, so they would still be observable by this 3+1 analysis [10].

An example for an atmospheric muon neutrino disappearance signature investigated by this analysis is shown in fig. 3. The parameters of the sterile neutrino have been chosen to be $\Delta m_{42}^2 = 0.5 \text{ eV}^2$, $\theta_{24} = 11^\circ$, because these values have not yet been excluded by other experiments, but are large enough to serve for illustrative purposes. In the antineutrino channel, a strong, resonant oscillation minimum can be seen at about 4 TeV for the particles that traversed the inner core of the Earth. The signature shifts to higher (lower) neutrino energies for larger (smaller) Δm_{42}^2 , and it becomes stronger and shifts closer to the horizon for larger θ_{24} .

4. Analysis Method

The aim of the analysis is to determine or to constrain θ_{24} and Δm_{42}^2 . This is accomplished by a forward-folding method where the measured muon neutrino rate as a function of reconstructed energy and direction is compared with expectations from simulation. We use a two-dimensional likelihood ratio test, binned in the reconstructed values for $\cos(\theta)$ and $\log_{10}(E_\mu)$:

$$\Lambda = \frac{\sup_{\hat{\xi}} \mathcal{L}(\theta_{24}, \Delta m_{42}^2, \hat{\xi})}{\sup_{\widehat{\theta_{24}}, \widehat{\Delta m_{42}^2}, \hat{\xi}} \mathcal{L}(\widehat{\theta_{24}}, \widehat{\Delta m_{42}^2}, \hat{\xi})}. \quad (4.1)$$

Here, \mathcal{L} denotes the likelihood, which is a standard Poissonian likelihood function of the event numbers in all bins, and sup indicates the maximized likelihood. The results were compared and verified with a likelihood formulation that also takes into account statistical uncertainties of the

simulated reference histograms [13]. ξ denotes an ensemble of nuisance parameters that are optimized independently at each point in the physics parameter space for best agreement with the experimental data [14].

For energies that are relevant for this analysis, the zenith angle θ can be measured with good accuracy, to better than one degree. The neutrino energy E_ν can be estimated by measuring the energy loss of its induced muon. The energy resolution is limited as the muon does not inherit the full energy of the neutrino, and the interaction might have happened far outside the detector such that the muon already lost a significant part of its energy. However, as this analysis employs forward folding, it does not rely on the individual values of the reconstructed neutrinos as long as the reconstruction algorithm behaves identical for the ensembles of experimental and simulated data. The data set is binned in two dimensions, with 25 bins in $\cos(\theta)$ and 13 bins in $\log_{10}(E_\mu)$.

The effects of systematic uncertainties on the expectation values of event rates in each zenith-energy bin have been parametrized and included into the likelihood function as continuous parametrizations of the corresponding nuisance parameters ξ . In contrast to the two physics parameters θ_{24} and Δm_{42}^2 , the fit results for nuisance parameters can not be considered to be measurements of the physical quantities as they are free parameters in the numerator and denominator of the likelihood ratio for every point of the likelihood scan. Furthermore, they can be highly degenerate in their effect on the description of the data. Their purpose is to account for all systematic uncertainties to avoid a bias in the measurement of the physics parameters.

The likelihood maximization is performed by a scan in the parameter range of $\Delta m_{42}^2 = 10^{-2.0} \dots 10^{0.7} \text{ eV}^2$ and $\theta_{24} = 0 \dots 42.5^\circ$, and the differences between two times the logarithmic likelihood (LLH) values Λ from (4.1) for a given pair of parameters and the point of best fit are then used as a test statistic. According to Wilks' theorem, this follows a χ^2 distribution with two degrees of freedom if the minimum of the LLH landscape can clearly be associated to a specific pair of parameters [15]. However, this precondition of Wilks' theorem is not strictly fulfilled for the null hypothesis, i.e., for the case that there are no sterile neutrinos mixing with muon neutrinos, and we have determined the small deviations from the predicted χ^2 distribution by ensemble tests. For the construction of confidence regions we use the more conservative test statistics from these ensemble tests.

5. Systematic Uncertainties

For this challenging measurement that relies on the agreement between simulated and measured distribution of energy and zenith, a correct handling of systematic uncertainties is crucial. Because of the large possible parameter space of sterile neutrinos, it is not possible to define an off-region that is known to be free of possible signal influence and could be used for the determination of nuisance parameters. At this point, most, but not yet all, relevant uncertainties are included, so the results are still preliminary. The nuisance parameters that are included are the total rate normalization, the cosmic-ray spectral index that affects the slope of the energy distribution, the kaon-pion ratio in cosmic-ray interactions that affects the angular distribution, the antineutrino-neutrino ratio that affects angular distribution and strength of the oscillation effect, and the relative optical efficiency of the light detection that affects the energy scale. All of them are implemented with a weak Gaussian prior, larger than or equal to the estimated uncertainty, to be particularly con-

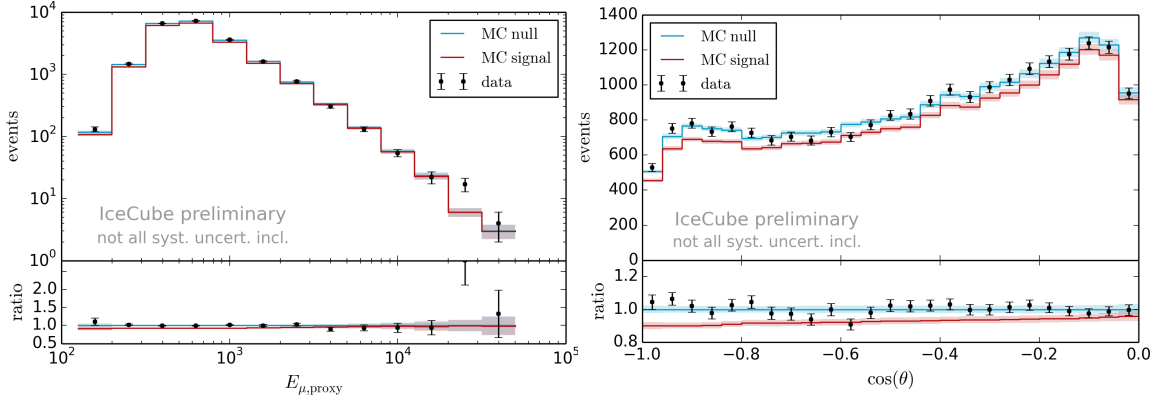


Figure 4: Distributions of reconstructed energy and reconstructed zenith angle, each marginalized over the other variable, respectively; the error band indicates the statistical uncertainty on the Monte-Carlo prediction. Shown are measured experimental data, as well as Monte-Carlo predictions for the null hypothesis and for our benchmark signal model from the previous figures. Note that for demonstration purposes the nuisance parameters have not been fitted for the benchmark model.

uncertainty	default value	prior
total rate normalization	1.00	0.40
cosmic-ray spectral index	2.65	0.05
cosmic-ray kaon-pion ratio	1.00	0.10
antineutrino-neutrino ratio	0.440	0.022
relative optical efficiency	1.00	—

Table 1: Nuisance parameters and their priors

servative in this first analysis and only to improve the numerical convergence of the fit; see table 1. The atmospheric neutrino flux is based on a parametrization of the model by [16], extending it to higher energy. This flux is modified by changes of the above nuisance parameters. In addition, small changes in the zenith distribution related to atmospheric temperature variations have been estimated based on satellite data and corrected for. Currently not included is a variation of the ice model parameters that describe the propagation of photons. This propagation is modeled according to [17] and a comparison with [18] is underway. Uncertainties on the Earth’s matter density and neutrino interaction cross-sections are negligible compared to other uncertainties and have not been included.

6. Results

Figure 4 shows the distribution of experimental data as marginalizations of the reconstructed zenith angle and energy distributions in comparison with the simulation of the null hypothesis with fitted nuisance parameters. The experimental result is well described with the simulation, excluding a strong disappearance signal. For comparison, the figure also includes predictions for the benchmark model described in section 3, with the same nuisance parameter values as fitted for the null hypothesis. The signature of this model is clearly distinguishable from the null hypothesis.

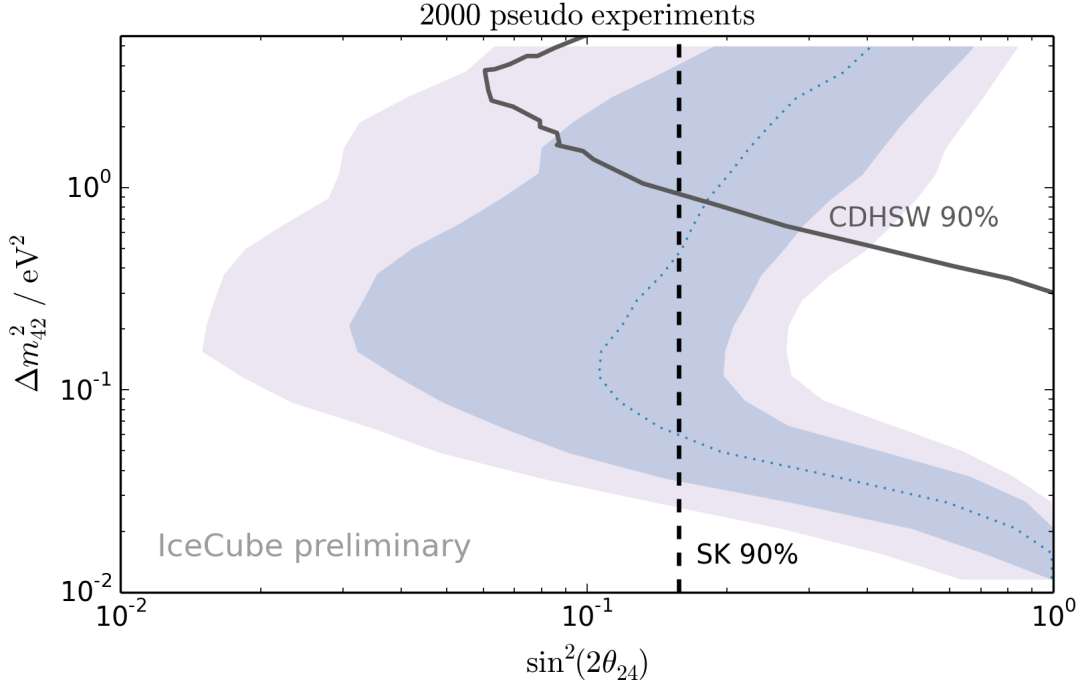


Figure 5: Expected region of 90% C.L. exclusion sensitivity of this analysis for the null hypothesis in comparison to the exclusion by other experiments [5][12]. For the Super-K contour, $\theta_{14} = 0$ was assumed. The contours are indicating the median (dotted curve), the 68% (darker blue) and 90% (lighter blue) ranges for the 90% C.L. exclusions from an ensemble of 2000 pseudo-experiments. Not all systematic uncertainties have been fully included yet.

When the nuisance parameters get fitted, the distributions become more similar, but the tension of the nuisance parameters with their expected values allows us to retain much of our sensitivity.

As discussed in section 3, this analysis is, unlike those of other experiments, primarily sensitive to the matter resonance effect. As a result, we expect fluctuations in the sensitivity for the vacuum oscillation parameters. In order to quantify these fluctuations we have analyzed a series of pseudo-experiments based on the simulated null hypothesis. Figure 5 shows this expected range of exclusions. In a Δm_{42}^2 range between 0.1 and 1 eV^2 , the analysis can significantly extend existing limits to values of $\sin^2(2\theta_{24}) = 0.1$ or even below. Experimental results will be reported soon.

7. Conclusion and Outlook

With the large statistics of well-reconstructed tracks induced from atmospheric muon neutrinos that IceCube measures each year, it is possible to search for disappearance effects caused by sterile neutrinos that mix with muon neutrinos. The energy- and zenith-dependent signature of these neutrino oscillations gets strongly enhanced by matter effects inside the Earth and increases IceCube’s sensitivity in the mass-splitting range of about $\Delta m_{42}^2 = 0.01 \dots 1.0 \text{ eV}^2$.

Here, the sensitivity of a first IceCube analysis are presented with data from IceCube in its 59-string configuration. The expected exclusion limits significantly constrain the allowed parameter space for sterile neutrinos and substantially improve previous limits. In the near future, an anal-

ysis based on IceCube data taken over multiple years with a selection optimized for the relevant energy range could further improve these limits significantly. The high sensitivity of this analysis demonstrates the good performance of IceCube and its capability to address fundamental questions of particle physics.

Acknowledgments

In addition to the general IceCube acknowledgments in the special section of these proceedings, we would like to thank the IT Center of the RWTH Aachen University for their grant of computing resources.

References

- [1] J. Beringer et al., *Phys. Rev. D* **86** (2012) 177-198 doi:10.1103/PhysRevD.86.010001.
- [2] A. Aguilar et al., *Phys. Rev. D* **64** (2001) 112007 doi:10.1103/PhysRevD.64.112007.
- [3] A.A. Aguilar-Arevalo et al., *Phys. Rev. Lett.* **110** (2013) 161801 doi:10.1103/PhysRevLett.110.161801.
- [4] R.W.L. Jones et al., *Phys. Rep.* **427** 5-6 (2006) 257-454 doi:10.1016/j.physrep.2005.12.006.
- [5] K.N. Abazajian et al., *Light Sterile Neutrinos: A White Paper*, hep-ph (2012) [arXiv:1204.5379].
- [6] M.G. Aartsen et al., *Phys. Rev. D* **89** 062007 (2014) doi:10.1103/PhysRevD.89.062007, [arXiv:1311.7048].
- [7] H. Nunokawa, O.L.G. Peres and R. Zukanovich Funchal, *Phys. Lett. B* **562** 279 (2003) [arXiv:hep-ph/0302039].
- [8] T.K. Kuo and J. Pantaleone, *Rev. Mod. Phys.* **61** (1989) 937-977 doi:10.1103/RevModPhys.61.937.
- [9] M. Wallraff and C. Wiebusch, *Calculation of oscillation probabilities of atmospheric neutrinos using nuCraft*, *Comput. Phys. Commun.* (forthcoming) [arXiv:1409.1387].
- [10] D. Hellwig and M. Wallraff, *Calculation of oscillation probabilities of atmospheric neutrinos with additional sterile mass states using nuCraft*, IceCube Internal Report (2013) icecube/201303001.
- [11] A. Esmaili, F. Halzen and O.L.G. Peres, *Exploring ν_τ - ν_s mixing with cascade events in DeepCore*, *JCAP* **1307** 048 (2013) [arXiv:1303.3294].
- [12] K. Abe et al., *Phys. Rev. D* **91** 052019 (2015) doi:10.1103/PhysRevD.91.052019.
- [13] D. Chirkin, *Likelihood description for comparing data with simulation of limited statistics*, *Instrumentation and Methods for Astrophysics* (2013) [arXiv:1304.0735].
- [14] G. Cowan et al., *EPJ C* **71** (2011) 1554 doi:10.1140/epjc/s10052-011-1554-0.
- [15] S.S. Wilks, *Ann. Math. Statist.* **9** (1938) 60-62 doi:10.1214/aoms/1177732360.
- [16] M. Honda, T. Kajita, K. Kasahara, S. Midorikawa and T. Sanuki, *Phys. Rev. D* **75**, 043006 (2007) [arXiv:astro-ph/0611418].
- [17] M.G. Aartsen et al., *Nucl. Instrum. Meth. A* **711** (2013) 73 [arXiv:1301.5361].
- [18] M.G. Aartsen et al., *Evidence of optical anisotropy of the South Pole ice*, 33nd ICRC (2013) [arXiv:1309.7010].